

# Deformation of the triangular spin- $\frac{1}{2}$ lattice in $\text{Na}_2\text{SrCo}(\text{PO}_4)_2$

Vera P. Bader,<sup>1,\*</sup> Jan Langmann,<sup>2</sup> Philipp Gegenwart,<sup>1</sup> and Alexander A. Tsirlin<sup>1,3,†</sup>

<sup>1</sup>*Experimental Physics VI, Center for Electronic Correlations and Magnetism,  
University of Augsburg, 86159 Augsburg, Germany*

<sup>2</sup>*Chemical Physics and Materials Science, University of Augsburg, 86159 Augsburg, Germany*

<sup>3</sup>*Felix Bloch Institute for Solid-State Physics, University of Leipzig, 04103 Leipzig, Germany*  
(Dated: August 12, 2022)

Crystal structure and thermodynamic properties of  $\text{Na}_2\text{SrCo}(\text{PO}_4)_2$ , the chemical sibling of the triangular quantum spin-liquid candidate  $\text{Na}_2\text{BaCo}(\text{PO}_4)_2$ , are reported. From single crystal x-ray diffraction and high-resolution synchrotron x-ray powder diffraction, the compound was found to crystallize in the monoclinic space group  $P2_1/a$  at room temperature, in contrast to the trigonal  $\text{Na}_2\text{BaCo}(\text{PO}_4)_2$ . Above 650 K, the symmetry of  $\text{Na}_2\text{SrCo}(\text{PO}_4)_2$  changes to  $C2/m$ , while around 1025 K a further transformation toward trigonal symmetry is observed. The monoclinic symmetry leads to a small deformation of the  $\text{CoO}_6$  octahedra beyond the trigonal distortion ubiquitous in this structure type, and results in the stronger  $g$ -tensor anisotropy ( $g_z/g_{xy} = 1.6$ ) as well as the increased XXZ anisotropy ( $J_z/J_{xy} = 2.1$ ) compared to the Ba compound ( $g_z/g_{xy} = 1.1$ ,  $J_z/J_{xy} = 1.5$ ), while the average coupling strength,  $J_{av}/k_B = (2J_{xy} + J_z)/3k_B \simeq 1.3$  K, remains unchanged. The Néel temperature increases from 140 mK (Ba) to 600 mK (Sr), and an uncompensated in-plane moment of  $0.066(4)\mu_B/\text{f.u.}$  appears. We show that the ordering temperature of a triangular antiferromagnet is capably controlled by its structural distortions.

## I. INTRODUCTION

The search for quantum spin-liquids in triangular antiferromagnets has its beginning with Anderson's transfer of Pauling's resonating valence bond model to spin-1/2 triangular Heisenberg antiferromagnets [1]. Later it was shown theoretically and experimentally that in this nearest-neighbor (nn) isotropic Heisenberg antiferromagnet long-range magnetic order in the form of a  $120^\circ$  non collinear ground state is realized instead [2, 3]. The same holds if the model is extended from the Heisenberg to the XXZ case by introducing an anisotropy parameter  $\Delta$  [4]. Luckily the prospects of a quantum spin liquid state in spin-1/2 triangular antiferromagnets (TLAF) are not over here because two further adjusting screws are available to push the system into a spin-liquid state [5]. One possibility is the introduction of off-diagonal anisotropy and another one is the addition of next-nearest-neighbor (nnn) interactions  $J_2$  [6–8]. However, it is still debated whether the off-diagonal anisotropy alone could stabilize a quantum spin liquid [9, 10], whereas already nnn interactions as small as 6% of the isotropic nn interaction can push the system into a spin-liquid state [6, 11, 12]. This offers a large playground for experimentalists who can try to tune their systems through the parameter space. Desirable are materials with undistorted triangular lattices and  $\Delta$  close to 1. Enhanced XXZ anisotropy leads to a narrowing of the spin-liquid window in the above described parameter range [11] which makes it more difficult to access the spin-liquid regime.

Existing theoretical works suggest that the spin-liquid state is unlikely to appear in a TLAF with vanishingly small  $J_2$ , especially if there are no pre-conditions for the large off-diagonal anisotropy. It is surprising from this perspective that the quantum spin-liquid state has been claimed in  $\text{Na}_2\text{BaCo}(\text{PO}_4)_2$  based on the absence

of static magnetism, as shown by the ac susceptibility measured down to 50 mK [13] and muon spin relaxation measured down to 80 mK [14].  $\text{Na}_2\text{BaCo}(\text{PO}_4)_2$  is a  $S = 1/2$  TLAF. The  $\text{Co}^{2+}$  ions with the effective spin-1/2 form a triangular lattice with the nn distance of around 5.3 Å. The magnetic layers in the  $ab$  plane are stacked along  $c$  and are separated by non-magnetic ions (similar to Fig. 1) [13]. Because there is no direct Co-O-Co link within the magnetic slabs, one exchange path is expected to be Co-O-P-O-Co, e.g., the magnetic coupling is mediated through the  $\text{PO}_4$  tetrahedra [15]. The large nnn distance of around 9.2 Å should lead to an insignificant exchange  $J_2$ , thus rendering  $\text{Na}_2\text{BaCo}(\text{PO}_4)_2$  a purely nearest-neighbor triangular antiferromagnet, which is not expected to host a quantum spin liquid. Later indeed, the picture of a spin-liquid ground state was challenged by the phase transition observed in zero-field heat capacity at 140 mK [16], but the low-temperature properties are still controversially discussed in the literature [16, 17].

In general, quantum states of matter hinge upon a delicate balance of competing interactions that depend, in turn, on fine details of the crystal structure. For example, in  $\text{Cs}_2\text{CuBr}_4$  the Jahn-Teller effect compresses the  $\text{CuBr}_4$  tetrahedra and the spin-1/2 ions form, as a consequence, a distorted triangular lattice. This leads to a small perturbation in the form of Dzyaloshinskii-Moriya (DM) interactions, which are supposed to be responsible for the stabilization of several plateau phases, whereas undistorted TLAFs, like  $\text{Ba}_3\text{CoSb}_2\text{O}_9$ , show the 1/3-plateau of the up-up-down magnetic phase only [18–21]. Not only the arrangement of the magnetic ions is crucial but also the non magnetic spacer ions can have a decisive influence on the properties. The 2D character of the system can be influenced by tuning the separation between the layers. Going from  $\text{Ba}_3\text{CoNb}_2\text{O}_9$  to  $\text{Ba}_8\text{CoNb}_6\text{O}_{24}$ , that means increasing the thickness of the non-magnetic buffer layer,

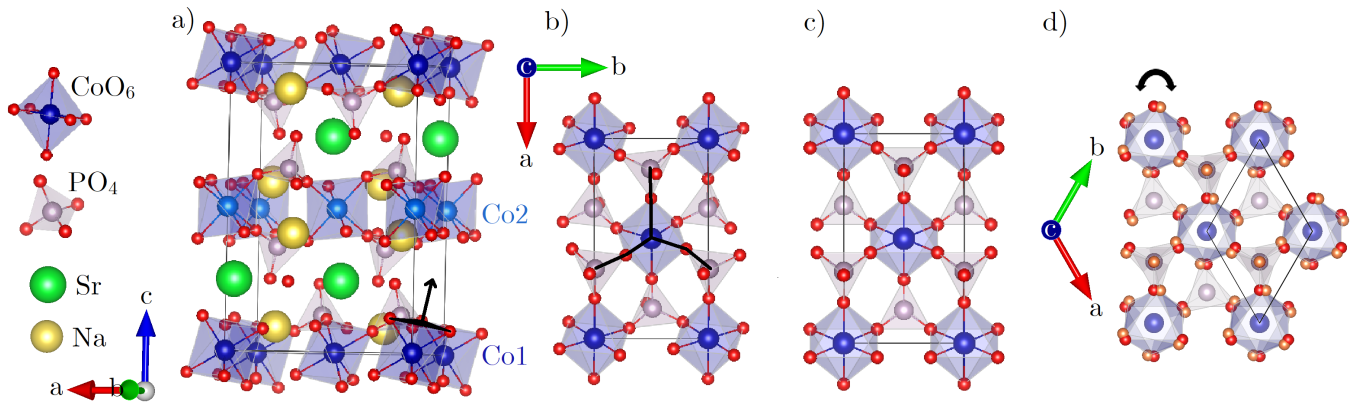


FIG. 1. Crystal structure of  $\text{Na}_2\text{SrCo}(\text{PO}_4)_2$ . (a) Unit cell viewed perpendicular to the  $c$  axis showing the layered structure. The tilting of the  $\text{CoO}_6$  octahedra is indicated with the black arrow. (b) Triangular layer formed by the  $\text{CoO}_6$  octahedra in the low-temperature monoclinic phase  $P2_1/a$  viewed along the  $c$  axis. The Co-O-P bonds referred to in Sec. III B are drawn with thick black lines. (c) Same triangular layer in the intermediate monoclinic phase  $C2/m$ . (d) Triangular layer in the high-temperature trigonal phase  $P\bar{3}m1$ . In the top view perspective, the  $\text{Na}^+$  and  $\text{Sr}^{2+}$  ions were omitted for clarity.

leads to the suppression of two subsequent phase transitions and formation of a single broad feature in the heat capacity data [22, 23].

Here, we study the sensitivity of the disputed quantum spin-liquid state of  $\text{Na}_2\text{BaCo}(\text{PO}_4)_2$  to structural changes induced by a chemical substitution. We show that the new compound,  $\text{Na}_2\text{SrCo}(\text{PO}_4)_2$  obtained by replacing Ba with Sr develops an antiferromagnetic order with a sizable uncompensated magnetic moment below 600 mK. This Néel temperature  $T_N$  is more than four times higher than in the Ba case, whereas the crystal structure of  $\text{Na}_2\text{SrCo}(\text{PO}_4)_2$  shows a clear monoclinic distortion that leads to a weak deformation of the triangular spin lattice and the enhanced easy-axis anisotropy.

## II. METHODS

### A. Sample preparation

The growth procedure is similar to the synthesis of  $\text{Na}_2\text{BaCo}(\text{PO}_4)_2$  reported in Ref. [13], albeit with several adjustments. Single crystals of  $\text{Na}_2\text{SrCo}(\text{PO}_4)_2$  were synthesized by mixing and grinding stoichiometric amounts of  $\text{Na}_2\text{CO}_3$  (99.999% Sigma-Aldrich),  $\text{SrCl}_2$  (anhydrous, 99.5 % Alfa Aesar),  $\text{Co}(\text{NO}_3)_2 \cdot 6\text{H}_2\text{O}$  (99.999% Sigma-Aldrich), and  $(\text{NH}_4)_2\text{HPO}_4$  (99% Grüssing GmbH) together with the NaCl flux (99.99% Alfa Aesar) (Co:Cl 1:25) in an Ar-glovebox. The ground powder was loaded in an alumina combustion boat and placed in a tube furnace with the  $\text{N}_2$  flow of 20 sccm during the synthesis. The sample was heated to  $850^\circ\text{C}$  and subsequently cooled to  $750^\circ\text{C}$  with the rate of 1.5 K/h. Pink crystals formed both in the boat and on the quartz tube. The amount and size of the crystals varied from one growth procedure to another, suggesting that other phases are in strong competition with  $\text{Na}_2\text{SrCo}(\text{PO}_4)_2$ .

The crystals were removed with tweezers and/or with distilled water and selected and cut under the microscope.

### B. Structural characterization

Single-crystal x-ray diffraction experiments were performed at room temperature on a translucent light pink and platelet-shaped crystal (*i*) before (dimensions  $76\ \mu\text{m} \times 306\ \mu\text{m} \times 413\ \mu\text{m}$ ) and (*ii*) after cutting with a scalpel (dimensions  $76\ \mu\text{m} \times 141\ \mu\text{m} \times 213\ \mu\text{m}$ ). The samples were attached to MiTeGen MicroMounts using perfluorinated polyether and mounted on a BRUKER Smart-Apex diffractometer featuring a D8 goniometer in fixed- $\chi$  geometry (BRUKER). Intensity data were collected in  $\omega$ -scanning mode ( $\Delta\omega = 0.5^\circ$ ) using an INCOATEC microfocus sealed-tube x-ray source ( $\text{AgK}\alpha$ ,  $\lambda = 0.56087\ \text{\AA}$ ) and a BRUKER APEX II CCD-detector. Detector-to-sample distances were chosen as 40 mm (*i*) and 50 mm (*ii*).

The as-cast sample (*i*) was affected by triple twinning, while the cut sample (*ii*) was a single domain. X-ray diffraction intensities for both samples were evaluated using the APEX2 [24] suite of programs and subjected to scaling and numerical absorption correction using the program SADABS [25]. Structural models were refined with the program JANA2006 [26]. Further information concerning the investigated samples, the collected x-ray diffraction data and the obtained structural model for sample (*ii*) are provided in Ref. [27]. The crystal structures were drawn in VESTA [28].

For high-resolution synchrotron x-ray powder diffraction measurements, fine powder was filled in a quartz capillary that was spun during the experiment. The powder sample was prepared by grinding single crystals. The measurements were performed at the ID22 beamline of the ESRF (Grenoble, France) with a wave-

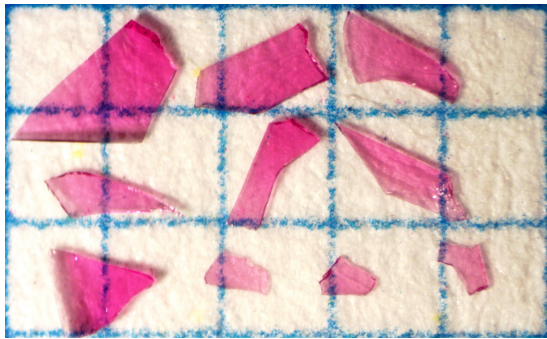


FIG. 2. Pink single crystals of  $\text{Na}_2\text{SrCo}(\text{PO}_4)_2$ .

length of  $0.35423 \text{ \AA}$  at different temperatures between 10 and 1025 K using He-flow cryostat (10 to 220 K),  $\text{N}_2$ -flow cryostream (150 to 450 K), and hot-air blower (450 to 1025 K). Structural models were refined with the program JANA2006 [26].

### C. Magnetization measurements

For magnetization measurements, the MPMS3 from Quantum Design was used. The data were collected using the DC option. In-plane and out-of-plane magnetization were measured on the same 0.15 mg single crystal. With a little amount of GE varnish the crystal was glued onto a quartz sample holder. The background contribution was negligible. In this setup, the temperature range from 2 to 400 K was covered. Temperatures down to 400 mK were obtained by using the  $^3\text{He}$  inset from Quantum Design. For this setup, the sample was glued into a plastic straw. The sample was centered at room temperature, cooled down to 400 mK, and centered again. In both configurations magnetization was measured up to 7 T.

### D. Heat capacity measurements

The heat capacity was measured by using the relaxation method in the PPMS from Quantum Design. After the addenda measurement of platform and low-temperature grease, the 0.23 mg single crystal was glued onto the platform. With the  $^3\text{He}$  option, measurements down to around 0.4 K were possible. Due to the light weight of the sample, the upper temperature was limited to 10 K. The data were collected for different fields ranging from 0 to 5 T.

### E. *Ab initio* calculations

Density-functional-theory (DFT) band-structure calculations were performed in the FPL0 [29] code using the Perdew-Burke-Ernzerhof (PBE) approximation for the exchange-correlation potential [30]. Lattice parameters

and atomic positions for  $\text{Na}_2\text{SrCo}(\text{PO}_4)_2$  were taken from the structure refinement against the single-crystal XRD data. The PBE calculations were used to assess orbital energies of  $\text{Co}^{2+}$ . Additionally, full-relativistic DFT+ $U$  was used to compute total energies of collinear spin configurations and obtain exchange couplings by a mapping procedure assuming  $S = \frac{3}{2}$  for  $\text{Co}^{2+}$ . The on-site Coulomb repulsion and Hund's coupling of DFT+ $U$  were chosen as  $U_d = 5 \text{ eV}$  and  $J_d = 1 \text{ eV}$ , respectively [17].

## III. RESULTS

### A. Room-temperature crystal structure

The pink single crystals of  $\text{Na}_2\text{SrCo}(\text{PO}_4)_2$  are shown in Fig. 2. The crystals are thin platelets, the largest ones having an area of approximately  $1 \text{ mm}^2$ . In contrast to trigonal  $\text{Na}_2\text{BaCo}(\text{PO}_4)_2$ , at room temperature  $\text{Na}_2\text{SrCo}(\text{PO}_4)_2$  crystallizes in the monoclinic symmetry, as evident from the peak splittings in the high-resolution XRD data shown in Fig. 3 [32]. The initial model was derived from the  $\text{Na}_2\text{BaCo}(\text{PO}_4)_2$  structure [13] by transforming the basis vectors as follows:  $\vec{a}' = \vec{a} - \vec{b}$ ,  $\vec{b}' = \vec{a} + \vec{b}$ , and  $\vec{c}' = 2\vec{c}$ . Using powder x-ray diffraction (PXRD) data the lattice constants at room temperature were refined to be  $a = 9.20152(2) \text{ \AA}$ ,  $b = 5.26593(1) \text{ \AA}$ ,  $c = 13.54116(2) \text{ \AA}$ , and  $\beta = 90.06613(12)^\circ$ .

Extinction conditions derived from powder and single-crystal x-ray diffraction (SCXRD) suggest the choice of a primitive space group and indicate the presence of a  $2_1$  screw axis  $\parallel \vec{b}$  and an  $a$  glide plane. Furthermore, comparison of structural refinements (PXRD and SCXRD) using the two space groups ( $P2/a$ ,  $P2_1/a$ ) leads to reasonable atomic parameters for  $P2_1/a$  (No. 14) only. The positions of allowed and forbidden reflections in reconstructed reciprocal-space planes from SCXRD data and the parameters obtained from the Rietveld refinement of the data collected at 300 K with the space group  $P2_1/a$  are listed in Ref. [27].

The unit cell of  $\text{Na}_2\text{SrCo}(\text{PO}_4)_2$  is shown in Figs. 1(a) and (b).  $\text{CoO}_6$  octahedra form planar triangular layers, which are stacked along the  $c$  axis. The  $\text{CoO}_6$  octahedra in the slabs are bridged by  $\text{PO}_4$  tetrahedra.  $\text{Na}^+$  ions fill the voids in the layers and the  $\text{Sr}^{2+}$  ions act as spacer ions and create a buffer layer, which separates the magnetic layers. These structural considerations hold for both  $\text{Na}_2\text{SrCo}(\text{PO}_4)_2$  and  $\text{Na}_2\text{BaCo}(\text{PO}_4)_2$ . In the latter case the larger  $\text{Ba}^{2+}$  ions separate the Co layers. As expected for the Sr case, the magnetic layers are closer to each other, with the Co-Co distance of  $6.77 \text{ \AA}$  along  $c$  compared to  $7.01 \text{ \AA}$  for the Ba compound at 300 K. We note that with respect to the starting  $\text{Na}_2\text{BaCo}(\text{PO}_4)_2$  structure from Ref. [13] an additional origin shift of  $(0 \ 0 \ 0.5)$  was necessary for  $\text{Na}_2\text{SrCo}(\text{PO}_4)_2$ . In this way, the Co1 atom is positioned at the origin  $(0 \ 0 \ 0)$  of the unit cell.

One key difference that leads to the lower monoclinic



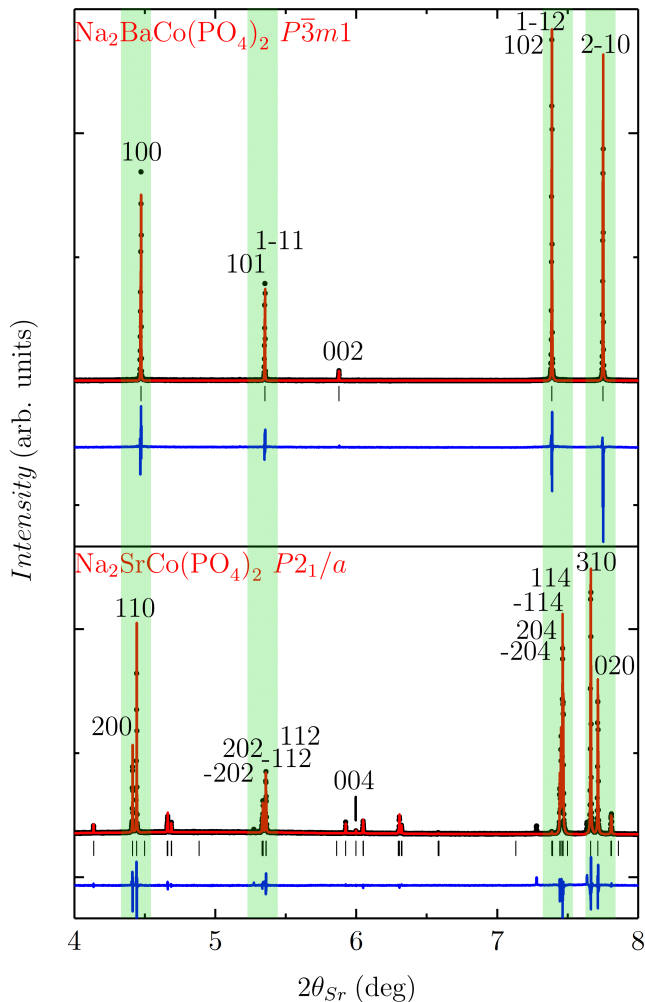


FIG. 3. Rietveld refinement for the synchrotron XRD data collected at 300 K in the trigonal space group for  $\text{Na}_2\text{BaCo}(\text{PO}_4)_2$  [31] and in the monoclinic space group  $P2_1/a$  for  $\text{Na}_2\text{SrCo}(\text{PO}_4)_2$ . The illustrated peak splitting is indicative of the monoclinic symmetry of the Sr compound. The scattering angles for  $\text{Na}_2\text{BaCo}(\text{PO}_4)_2$  were renormalized for an easier comparison with the Sr compound.

symmetry of the Sr compound compared to the trigonal symmetry of the Ba compound is the cooperative tilting of the  $\text{CoO}_6$  octahedra and  $\text{PO}_4$  tetrahedra. Different tilting in two adjacent layers causes the doubling of the unit cell along  $c$ .

Another difference is that the symmetry lowering allows distortions of the  $\text{CoO}_6$  octahedra with the local symmetry of the  $\text{Co}^{2+}$  ion reduced from  $D_{3d}$  to  $C_i$ . The trigonal distortion, captured by taking the O-Co-O angle with the largest deviation from  $90^\circ$ , is 4.8(2)% in the Ba compound and amounts to a maximum deviation of 6.0(3)% and 7.9(3)% for the  $\text{Co1O}_6$  and  $\text{Co2O}_6$  octahedra in the Sr compound, respectively. Additionally, symmetry lowering leads to three different Co-O lengths in the Sr compound compared to only one in the Ba compound.

This distortion beyond trigonal, i.e. the maximum deviation from the mean distance of the three Co-O bonds ( $d_1$ ,  $d_2$ , and  $d_3$ , see Fig. 10) is 1.5(7)% in the  $\text{Co1O}_6$  octahedra and 2.2(7)% in the  $\text{Co2O}_6$  octahedra. For the  $\text{PO}_4$  tetrahedra the symmetry reduces from  $C_{3v}$  to  $C_1$ . In the Ba compound, the  $\text{Co}^{2+}$  ions form a triangular lattice with equilateral triangles, whereas in the distorted Sr compound, the triangles are not equilateral but isosceles with one Co-Co distance being around 0.7% shorter compared to the two other distances at room temperature.

## B. Structural phase transitions

In this section, we investigate the temperature dependence of the crystal structure because several aspects indicate a structural phase transition. Since  $\text{Na}_2\text{SrCo}(\text{PO}_4)_2$  is a derivative of  $\text{Na}_2\text{BaCo}(\text{PO}_4)_2$ , the distortion may be reverted upon heating. In addition, the triple twinning of the crystal structure seen in the SCXRD data indicates that  $\text{Na}_2\text{SrCo}(\text{PO}_4)_2$  grows in a higher symmetry and then transforms into monoclinic upon cooling. A structural change from monoclinic to trigonal was already reported for different glaserite-type compounds [33–37].

To probe structural phase transitions, the synchrotron x-ray patterns at different temperatures between 10 and 1025 K were collected [32, 38]. No anomalies were observed below 650 K, except for a small peak in the monoclinic angle  $\beta$  at 200 K [Fig. 4(a)]. Since none of the  $a$ ,  $b$ ,  $c$  lattice parameters show any anomaly at this temperature [Fig. 4(c)], nor any feature is visible in the susceptibility and Fisher’s heat capacity [Figs. 7 and 4(a)], we believe that this small peak may be a measurement artifact caused by the change in the sample environment. On the other hand, prominent changes take place at 650 K. Above this temperature, the symmetry remains monoclinic, but some of the reflections disappear. The comparison of the data collected at 500 and at 800 K is shown in Fig. 4(b). The reflections labeled in black vanish above 650 K. The new extinction condition  $h + k = 2n$  is indicative of the  $C$  centering. A continuous evolution of the unit-cell volume [inset of Fig. 4(c)] further suggests that the transition is of second order and should thus follow the group-subgroup relation. From all these considerations, the space group with the highest possible symmetry is  $C2/m$ . The top view of the unit cell is shown in Fig. 1(c). In  $P2_1/a$  the tilting angle is the same for the  $\text{CoO}_6$  octahedra in one layer but opposite components of the tilting vector in the  $b$  direction forbid the vector  $(0.5 \ 0.5 \ 0)$  as a translational symmetry element. In contrast, in  $C2/m$  the  $b$  component vanishes, confining the tilting to the  $ac$  plane. The octahedra within the layers tilt the same way and the unit cell becomes  $C$ -centered. The  $c$  doubling is still present in the structure. Rietveld refinement of the exemplarily chosen data at 800 K in the space group  $C2/m$  describes the data accurately and is shown, together with the refined atomic

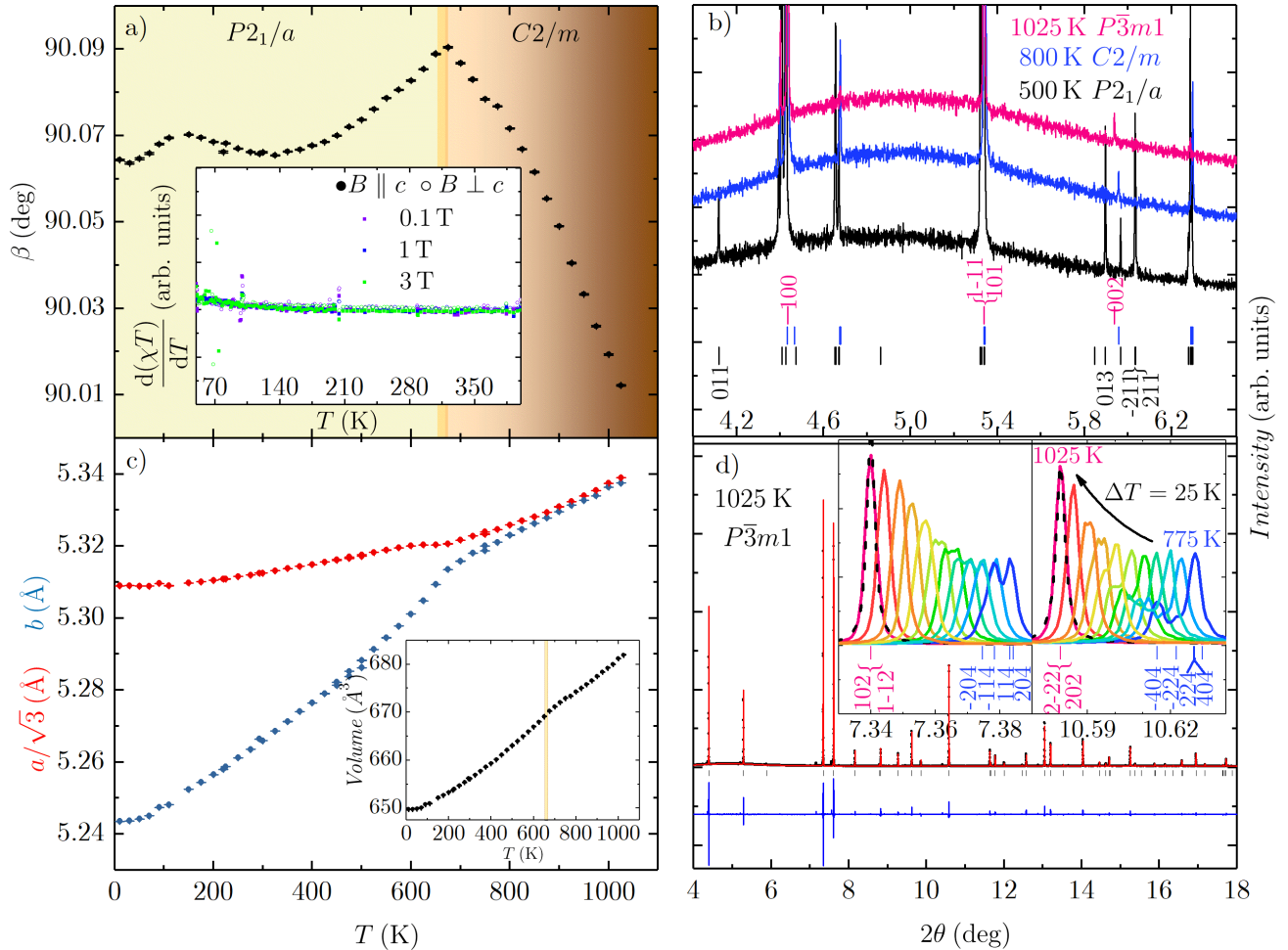


FIG. 4. Crystal structure of  $\text{Na}_2\text{SrCo}(\text{PO}_4)_2$  as a function of temperature. (a) Temperature dependence of the monoclinic angle  $\beta$ . The weak anomaly at 200 K is likely a measurement artifact, because thermodynamic measurements, including Fisher’s heat capacity  $d(\chi T)/dT$  (inset), reveal no anomaly at this temperature. The second anomaly at around 650 K marks the structural transition from the space group  $P2_1/a$  to  $C2/m$ . The color gradient marks the gradual transition to a trigonal space group which is not fully completed at 1025 K. (b) Synchrotron XRD data for selected temperatures illustrating the symmetry changes. The reflections labeled in black vanish for  $C2/m$  and the red labels indicate the remaining reflections for  $P\bar{3}m1$ . The scattering angles were rescaled with respect to the data collected at 500 K. (c) Red are the refined  $a/\sqrt{3}$  and blue are the refined  $b$  lattice parameters. Visible is the kink at the phase transition from  $P2_1/a$  to  $C2/m$  at around 650 K in both lattice parameters. At higher temperatures  $a/\sqrt{3}$  and  $b$  converge due to the transition into a trigonal structure. The inset shows the continuous change of the unit cell volume with temperature. (d) Rietveld refinement for the synchrotron XRD data collected at 1025 K in the trigonal space group  $P\bar{3}m1$ . The insets show the merging of the split peaks as the temperature increases.

parameters, in the Supplemental Material [27]. The observed phase transformation to  $C2/m$  was reversible and the room-temperature phase  $P2_1/a$  was recovered upon cooling.

On further increasing temperature, the values of the  $a/\sqrt{3}$  and  $b$  lattice parameters converge. The  $a/\sqrt{3}$  and  $b$  converging and the monoclinic angle  $\beta$  approaching  $90^\circ$ , both indicate the transition to a trigonal symmetry. The  $C2/m$  space group can be regarded as intermediate step in the  $P2_1/a$  to  $P\bar{3}m1$  transition series [39]. This is illustrated in Fig. 4(b), in which the red labels indicate the remaining reflections for  $P\bar{3}m1$ . That symmetry

constrains  $a/\sqrt{3}$  and  $b$  to be equal and restricts  $\beta$  to  $90^\circ$  becomes clear from the fact that many split peaks merge. This is shown in the inset of Fig. 4(d) for selected peaks. The clearly separated peaks at 775 K merge as the temperature is increased until the splitting cannot be resolved anymore at around 1000 K. At 1025 K,  $\beta$  has not reached  $90^\circ$  but equals  $90.0122(2)^\circ$ . The transition is not yet completed at 1025 K but the data can be also refined in the space group  $P\bar{3}m1$  by taking into account residual broadening via the increased reflection width. In this way, the diffraction pattern can be described accurately with a residue value  $R_p = 9.36\%$  [Fig. 4(d)], which

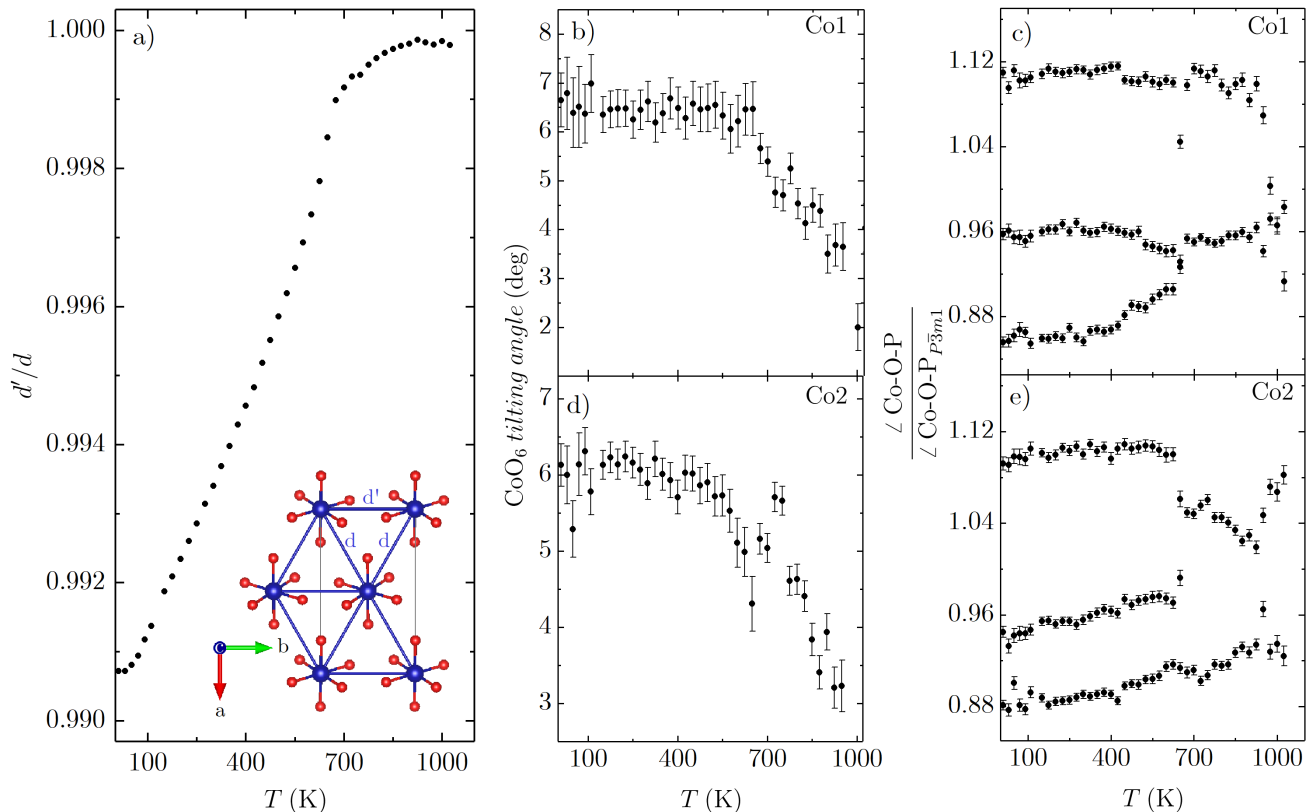


FIG. 5. Deviation from the trigonal structure. (a) The ratio of short ( $d'$ ) to long ( $d$ ) Co-Co bonds gauges deformation of the triangular lattice. The error bars are smaller than the symbol size. [(b) and (d)] Tilting angles of the  $\text{Co1O}_6$  and  $\text{Co2O}_6$  octahedra, respectively. [(c) and (e)]  $\text{Co1-O-P}$  and  $\text{Co2-O-P}$  angles, respectively. The angles were normalized in respect to the angle in the trigonal case.

is only slightly higher than the residue value of the refinement in the monoclinic structure ( $R_p = 8.59\%$ ). The Lorentzian parameter of the peak-shape function  $LY$  has the value of  $0.0412(2)^\circ$  for the refinement in the trigonal space group compared to  $LY = 0.0352(2)^\circ$  for the refinement in the monoclinic model. The atomic parameters in the trigonal space group are listed in Ref. [27]. We believe that at 1025 K,  $\text{Na}_2\text{SrCo}(\text{PO}_4)_2$  is on the verge of a phase transition into the trigonal structure. Unfortunately, technical reasons prevented us from performing measurements at even higher temperatures where peak broadening due to the minute monoclinic distortion could be fully suppressed.

The results from room-temperature SCXRD experiments also hint at the proximity of monoclinic  $\text{Na}_2\text{SrCo}(\text{PO}_4)_2$  to the trigonal aristotype structure with the space group  $P\bar{3}m1$ : An as-cast sample was subject to growth twinning with three monoclinic domains (space group  $P2_1/a$ ; domain fractions 87.5(3)% : 6.6(2)% : 5.9(3)%) and twin element  $\bar{3}$  oriented parallel to the  $c$  axis of the trigonal unit cell (see Ref. [27]). Cutting with a scalpel resulted in a single-domain sample underlining the macroscopic nature of the twin domains.

The  $P\bar{3}m1$  unit cell is shown in Fig. 1(d). As described

above the structure is undistorted and the polyhedra are not tilted. In the Sr compound ferrorotations of the  $\text{CoO}_6$  octahedra can be easily introduced in the magnetic layers which is illustrated in Fig. 1. The x rays record the average  $P\bar{3}m1$  structure.

The distortions appearing on cooling can be quantified by the ratio of the short ( $d'$ ) and long ( $d$ ) nearest-neighbor Co-Co distances. This ratio is depicted in Fig. 5(a). With increasing temperature the difference in length decreases and the structural phase transition at 650 K is apparent from the change of the slope. In  $C2/m$  the distortions still forbid trigonal symmetry but the triangles are nearly equilateral and the ratio approaches 1.0 which corresponds to the undistorted lattice in the  $P\bar{3}m1$  case.

The tilting of the  $\text{CoO}_6$  octahedra, indicated in Fig. 1(a) and shown in Figs. 5(b) and 5(d), is quantified by the angle between the normal of the indicated face of the octahedron and the  $c$  axis. In the untilted case ( $P\bar{3}m1$ ), the angle is  $0^\circ$ . In the space group  $P2_1/a$ , the octahedra are tilted the most, and in both Co layers the tilting angle stays nearly constant with temperature. After the phase transition to  $C2/m$  at around 650 K, the angles decrease until they reach at 1000 K around  $3^\circ$ ,

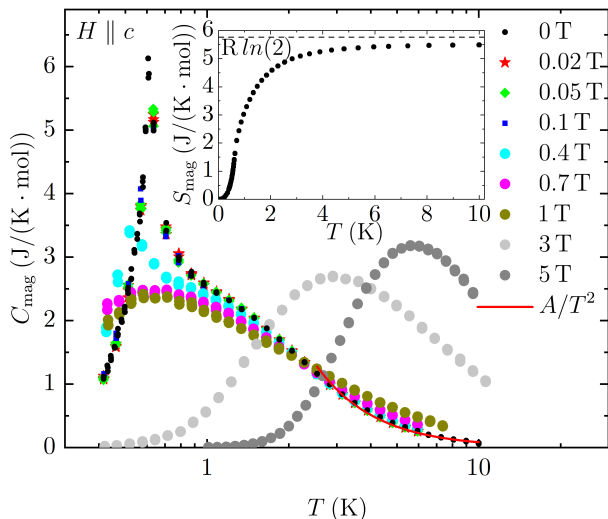


FIG. 6. Temperature dependence of the magnetic heat capacity at different magnetic fields parallel to  $c$ . The broad Schottky-like peak shifts to higher temperatures with increasing magnetic field. In low magnetic fields the broad peak due to short-range order is superimposed on the  $\lambda$ -type anomaly that indicates the magnetic ordering transition at 600 mK. The fit of the zero-field data is depicted as red line. The inset shows the zero-field magnetic entropy, which approaches  $R\ln(2)$ .

which is half the starting value.

The tilts of both  $\text{CoO}_6$  octahedra and  $\text{PO}_4$  tetrahedra affect the Co-O-P angles, which are visualized in Fig. 1(b). The Co-O-P unit is part of the magnetic exchange path and the temperature dependent Co-O-P bond angles are shown in Figs. 5(c) and 5(e). In the untilted case ( $P\bar{3}m1$ ) all the angles are the same and the depicted angles for different temperatures are normalized in regard to that value obtained at 1025 K. A larger deviation from the reference value is observed at the lowest temperatures. The three different angles indicate that the superexchange paths are different. With increasing temperature the spread of the angles decreases until two angles in each Co layer merge at the  $C2/m$  phase transition. The two different angles would finally coincide when the transition to  $P\bar{3}m1$  is completed.

### C. Heat capacity

The magnetic specific heat (after phonon subtraction) measured on a single crystal in different magnetic fields is shown in Fig. 6. In zero field, a sharp peak at around  $T_N \simeq 600$  mK indicates long-range magnetic order. Additionally, a hump centered around 1 K indicates short-range magnetic order above  $T_N$ , as typical for low-dimensional and frustrated antiferromagnets. On increasing the field,  $T_N$  initially does not change and then decreases to 520 mK at 0.4 T. In higher fields, only a

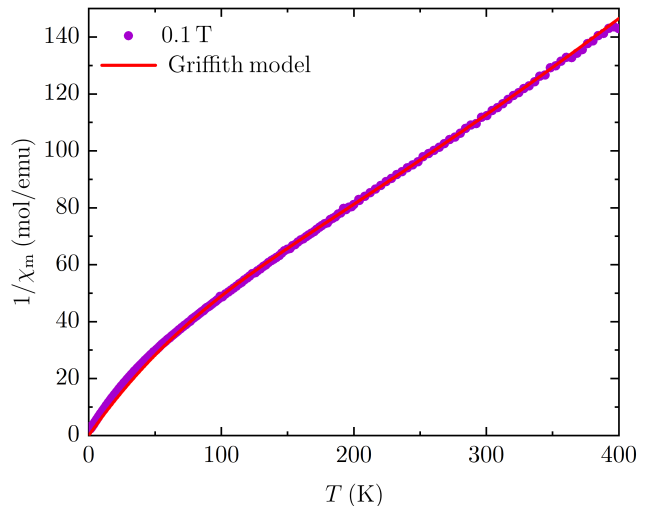


FIG. 7. Inverse magnetic susceptibility data at 0.1 T. The red line depicts the fit with the Griffith model as described in Ref. [43].

broad maximum remains, while  $T_N$  is suppressed below 0.4 K or vanishes. This behavior is broadly consistent with theoretical results for classical triangular antiferromagnets [40] and with experimental results obtained on model compounds, such as  $\text{Ba}_3\text{CoSb}_2\text{O}_9$  [41]. One noteworthy feature is that  $T_N$  drops by 13% at only 20% of the saturation field, i.e., it is suppressed faster than in other triangular antiferromagnets.

In fields above 1 T, the broad maximum systematically shifts toward higher temperatures and resembles a Schottky anomaly, suggesting that a fully polarized state has been reached, and the field-induced gap opens. Indeed, our magnetization data suggest saturation around 2 T (Fig. 9).

The phonon contribution was extracted by fitting the zero-field data between 2.5 to 10 K to  $B \cdot T^3 + A/T^2$  (see Ref. [27] and Fig. 6), where the first term is the phonon part and the second one is the lowest-order term in the high-temperature series expansion (HTSE) for the magnetic specific heat [42] ( $B = 2.6(2) \cdot 10^{-4} \text{ J}/(\text{K}^4 \cdot \text{mole})$ ,  $A = 8.3(1) \text{ (J} \cdot \text{K)/mole}$ ). In the nearest-neighbor triangular antiferromagnet,  $A = (9/16) \cdot R \cdot J^2$  and  $J/k_B = 1.33(1) \text{ K}$  is obtained. We will see that this value matches well to those determined in Sec. III D.

Before calculating the entropy by integration, the zero field data were extrapolated to 0 K using the proportionality  $C \propto T^3$  assuming a gapless antiferromagnet. The entropy is shown in the inset of Fig. 6 and approaches the value  $R\ln(2)$  expected for a spin-1/2 system. The small deviation of 5% may be caused by the weighing error for the small single crystal. This indicates that below 10 K,  $\text{Na}_2\text{SrCo}(\text{PO}_4)_2$  features effective spin-1/2 magnetic moments, similar to  $\text{Na}_2\text{BaCo}(\text{PO}_4)_2$ .

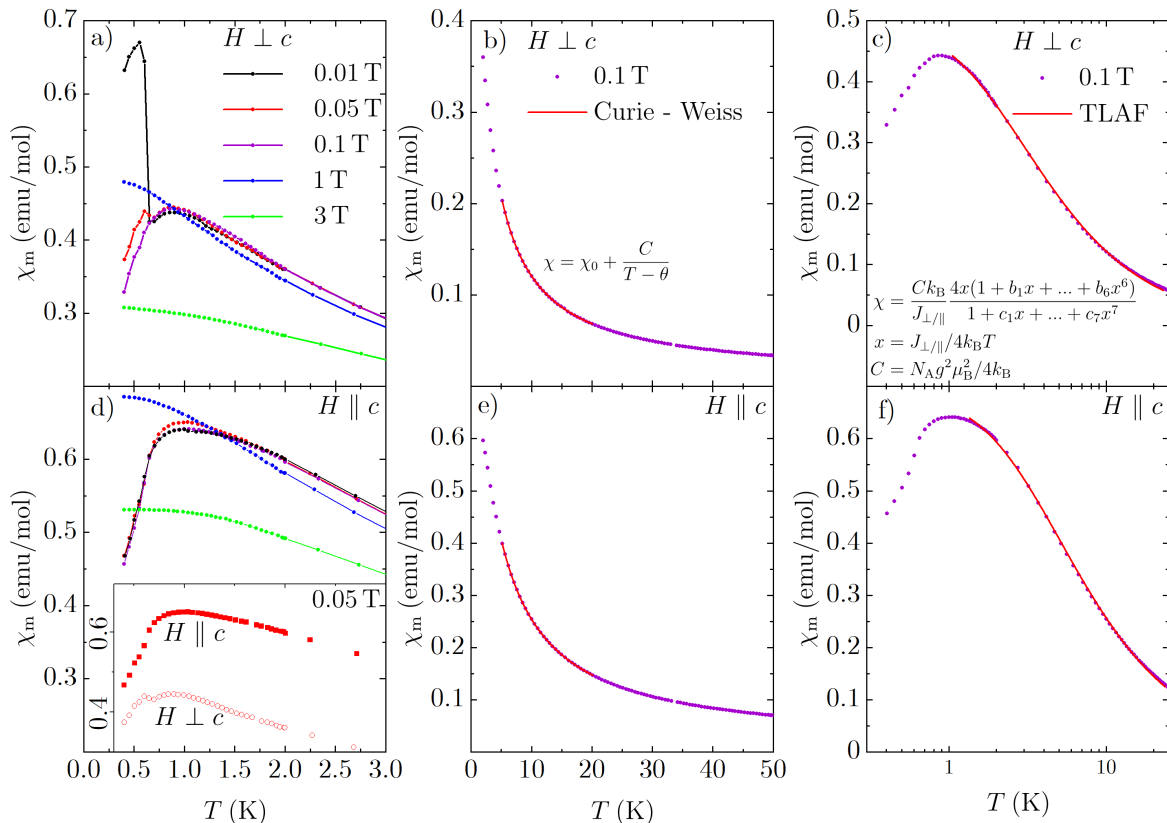


FIG. 8. (Top) Magnetic field perpendicular to  $c$ . (Bottom) Magnetic field parallel to  $c$ . [(a) and (d)] Magnetic susceptibility for different magnetic fields below 3 K. The antiferromagnetic transition manifests itself by the drop of the susceptibility and remains visible up to at least 0.1 T. The inset contrasts the susceptibilities for both field directions at 0.05 T. In low fields up to 0.05 T, the increase of the susceptibility below  $T_N$  for  $H \perp c$  originates from small uncompensated moments in the  $ab$  plane. [(b) and (e)] Curie-Weiss fits of the susceptibility between 5 and 20 K. [(c) and (f)] The TLA fit of the magnetic susceptibility describes the data accurately. The coefficients are listed in Ref. [44].

#### D. Magnetization

$\text{Co}^{2+}$  is a magnetic ion with the electronic configuration  $d^7$  and octahedral coordination in  $\text{Na}_2\text{SrCo}(\text{PO}_4)_2$ . In the high-spin case, spin-orbit coupling (SOC) lifts the degeneracy of the  $^4T_1$  dodecet. The lowest Kramers level has effective spin-1/2. The higher-lying Kramers levels have effective spin-3/2 and 5/2. At low temperatures only the low-lying doublet is accessed and an effective spin-1/2 behavior is observed, as confirmed by our analysis of the specific heat. With increasing temperature the higher-lying level with effective spin-3/2 gets populated [17]. In the temperature dependence of the inverse susceptibility (Fig. 7) the inflection point at around 70 K marks the increased population of the excited state. The model from Griffith [43] for  $d^7$  high-spin octahedral complexes describes the experimental data accurately but the theory has also its limitations. In our case, the obtained SOC-constant of 1377(11) K is around 2.5 times larger than in Ref. [17]. The model assumes an ideal octahedral symmetry wherein the splitting of the  $\text{Co}^{2+}$  multi-

plet arises from the SOC only. On the other hand, in  $\text{Na}_2\text{SrCo}(\text{PO}_4)_2$  trigonal distortion, as well as the deformation of the octahedra beyond trigonal symmetry, should lead to a crystal-field splitting of the  $t_{2g}$  levels (see also Sec. III E) and, consequently, to deviations from the simplified model by Griffith [43].

We now concentrate on the temperature range below 20 K where the influence of the excited states should be negligible and the pure spin-1/2 regime can be assumed. The Curie-Weiss fits,  $\chi = \chi_0 + C/(T - \theta)$ , between 5 and 20 K return the Curie-Weiss temperature  $\theta_{CW} = -3.07(3)$  K, Landé factor  $g = 5.8(3)$ ,  $\chi_0 = 7.8(5) \cdot 10^{-3}$  emu/mol for  $H \parallel c$  and  $\theta_{CW} = -1.44(3)$  K,  $g = 3.7(2)$ ,  $\chi_0 = 8.5(3) \cdot 10^{-3}$  emu/mol for  $H \perp c$  [Figs. 8(b) and 8(e)]. In both cases,  $g$  values are given for the effective spin-1/2 of the ground-state Kramers doublet.  $\chi_0$  was added to account for a Van-Vleck contribution. From  $\theta_{CW} = 1.5J/k_B$  for nearest-neighbor triangular antiferromagnets,  $J_z/k_B = 2.05(3)$  K and  $J_{xy}/k_B = 0.96(2)$  K are obtained. The average value  $J_{av}/k_B = (2J_{xy} + J_z)/3k_B = 1.32(3)$  K matches perfectly



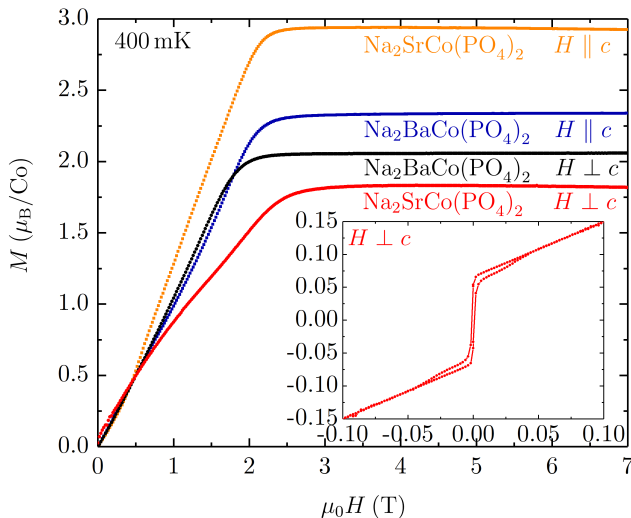


FIG. 9. Comparison of the magnetization versus magnetic field for  $\text{Na}_2\text{SrCo}(\text{PO}_4)_2$  and  $\text{Na}_2\text{BaCo}(\text{PO}_4)_2$  [31] for both field directions at 400 mK. The Sr compound shows a three times larger magnetic anisotropy. The inset shows the small hysteresis that indicates the uncompensated spin component in the  $ab$  plane.

the value extracted from the heat capacity data. The large difference of the  $g$  values indicates an anisotropy of around 37%. A similar anisotropy is obtained from saturation magnetization,  $M_s = g\mu_B S$ , measured at 0.4 K:  $g = 5.9(3)$  for  $H \parallel c$ ,  $g = 3.7(2)$  for  $H \perp c$ . In contrast, a much smaller anisotropy of 12% ( $g = 4.7(3)$  for  $H \parallel c$ ,  $g = 4.1(2)$  for  $H \perp c$ ) was measured for the Ba compound (Fig. 9). In the case of an undistorted  $\text{CoO}_6$  octahedron, one expects the isotropic value of  $g = 4.33$  assuming the effective spin-1/2. The disparity between  $g_z$  and  $g_{xy}$  is rooted in the distortion of the  $\text{CoO}_6$  octahedra. The relatively weak anisotropy in  $\text{Na}_2\text{BaCo}(\text{PO}_4)_2$  is caused by the trigonal distortion of only 4.6% at 10 K. The larger trigonal distortions of around 5.4% ( $\text{Co1O}_6$ ) and 8.8% ( $\text{Co2O}_6$ ) and the distortions beyond trigonal of around 2.6% ( $\text{Co1O}_6$ ) and 2.9% ( $\text{Co2O}_6$ ) in the Sr compound at 10 K are the origin for the larger  $g$  anisotropy.

The transition at 600 mK seen in the specific heat is due to an antiferromagnetic order, because it appears in the susceptibility too [see Fig. 8(a) and 8(d)]. The transition is observed in magnetic fields up to 0.1 T and is suppressed at 1 T. We note in passing that the magnetization curves measured at 400 mK show some nonlinearities for both directions of the applied field. These effects may indicate the formation of intermediate phases, such as the 1/3-plateau known from other triangular antiferromagnets, and affect the field evolution of  $T_N$ . However, measurements at much lower temperatures would be needed to resolve these intermediate phases. Such measurements lie beyond the scope of our present study.

On the other hand, our data shed light on the nature of the magnetic order in low fields. In the field

of 0.01 T, we observe a drastically different behavior depending on the direction of the applied field. Below  $T_N$ , the susceptibility decreases for  $H \parallel c$  and abruptly increases for  $H \perp c$ . This behavior can be compared to the textbook case of an easy-axis antiferromagnet where the susceptibility decreases in the field applied along the easy axis and becomes temperature-independent in the field applied perpendicular to the easy axis. Considering  $g_z > g_{xy}$  and the stronger exchange couplings manifested by the more negative Curie-Weiss temperature for  $H \parallel c$ , we identify  $c$  as the easy direction. Indeed, the evolution of the susceptibility below  $T_N$  suggests a large and fully compensated spin component along  $c$ . Additionally, an uncompensated spin component is expected in the  $ab$  plane, similar to Refs. [45, 46]. It leads to the abrupt increase in the susceptibility below  $T_N$  and further manifests itself by the hysteretic behavior in  $M(H)$ . The hysteresis is shown in the inset of Fig. 9 and the in-plane moment obtained from the saturation magnetization is  $\mu_{\text{Co}^{2+}} = 0.066(4)\mu_B/\text{f.u.}$ . This is equal to 3.5% of the out-of-plane saturated moment for  $B \perp c$ . Overall, our data are consistent with the Y-type spin pattern expected in XXZ triangular antiferromagnets with the large easy-axis anisotropy [47]. The uncompensated  $ab$ -component would arise if the Y pattern is slightly turned toward the  $ab$  plane. A neutron scattering study would be interesting in order to verify this conjecture.

In low-dimensional systems or frustrated antiferromagnets, short-range magnetic order often manifests itself by a broad hump in the magnetic susceptibility [48]. For spin-1/2 TLAFs, the broad hump can be described by a Padé approximated high-temperature series expansion with  $g$  and the exchange coupling  $J$  as adjustable parameters [44, 49]. The corresponding fits of the data below 25 K collected at 0.1 T are shown in Figs. 8(c) and 8(f) and yield the exchange interaction  $J_z/k_B = 1.76(1)$  K and  $g = 5.9(2)$  for  $H \parallel c$  and  $J_{xy}/k_B = 1.04(1)$  K and  $g = 3.9(1)$  for  $H \perp c$ . The thus obtained  $g$  values match the values from the Curie-Weiss fits and  $M(H)$  measurements.  $J_z$  and  $J_{xy}$  are in good agreement with the values from the Curie-Weiss fits and the average  $J_{\text{av}}/k_B = 1.28(1)$  K matches the value obtained from the specific heat data. The good description of the susceptibility data with the XXZ model suggests that any off-diagonal anisotropy terms should be small. Indeed, Ref. [50] arrives at a similar conclusion for  $\text{Na}_2\text{BaCo}(\text{PO}_4)_2$  using extensive numerical simulations and comparisons to the experimental data also at temperatures well below  $J_{\text{av}}$ .

### E. *Ab initio* results

PBE band structure of  $\text{Na}_2\text{SrCo}(\text{PO}_4)_2$  is metallic because electronic correlations relevant to a Mott insulator are not taken into account. A comparison to  $\text{Na}_2\text{BaCo}(\text{PO}_4)_2$  (Fig. 10) shows the nearly unchanged bandwidth that implies a similar strength of exchange couplings in the Sr and Ba compounds. On the other

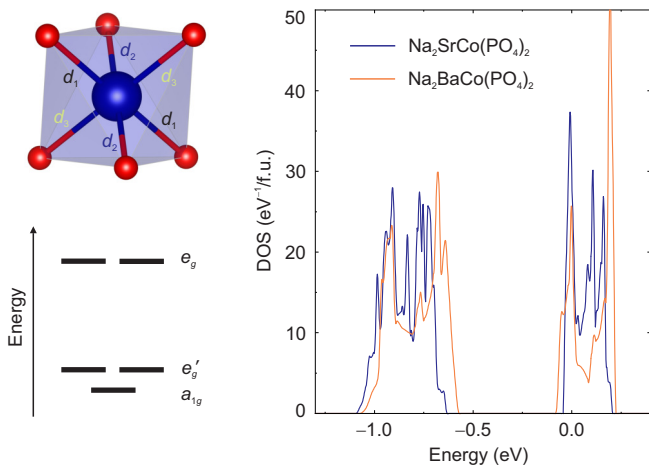


FIG. 10. Local distortions of the  $\text{CoO}_6$  octahedra, crystal-field splitting of  $3d$  orbitals, and the corresponding density of states for  $\text{Na}_2\text{SrCo}(\text{PO}_4)_2$  and  $\text{Na}_2\text{BaCo}(\text{PO}_4)_2$ . The Fermi level is at zero energy. Note that calculations are performed on the PBE level, resulting in the metallic band structures.

hand, re-structuring of both bands and density of states clearly indicates the increasing distortion of the  $\text{CoO}_6$  octahedra in the Sr compound.

Orbital energies summarized in Table I show that trigonal distortion of the  $\text{CoO}_6$  octahedra leads to the crystal-field splitting of 0.1 eV within the  $t_{2g}$  levels. The lower energy of the  $a_{1g}$  orbital corresponds to an easy-axis anisotropy of the  $g$  tensor [51], in agreement with the experimental  $g_z > g_{xy}$ . This splitting is almost unchanged in  $\text{Na}_2\text{SrCo}(\text{PO}_4)_2$ , but an additional splitting between the two  $e'_g$  levels appears. Therefore we conclude that the enhanced  $g$ -tensor anisotropy in  $\text{Na}_2\text{SrCo}(\text{PO}_4)_2$  should be related not to the trigonal distortion but to the distortion beyond trigonal.

Despite the fact that Co1 and Co2 are two distinct positions in the crystal structure of  $\text{Na}_2\text{SrCo}(\text{PO}_4)_2$ , their crystal-field splittings are almost the same, suggesting that experimental  $g$  values averaged over Co1 and Co2 should reflect the  $g$  values for each of the Co sites. The same is true for the nearest-neighbor exchange couplings evaluated using the mapping procedure. We find  $J_{\text{Co1}}/k_B = 1.5 \text{ K}$  and  $J_{\text{Co2}}/k_B = 1.8 \text{ K}$ . Therefore, average exchange coupling extracted from the HTSE fits should be indicative of the interaction strength in each of the triangular planes.

#### IV. DISCUSSION AND SUMMARY

To explain the measured data and to understand the different properties of  $\text{Na}_2\text{SrCo}(\text{PO}_4)_2$  and  $\text{Na}_2\text{BaCo}(\text{PO}_4)_2$ , we need to start by comparing the crystal structures of both compounds. The smaller atomic radii of the  $\text{Sr}^{2+}$  ions compared to the  $\text{Ba}^{2+}$  ions in the buffer layers lead to a decrease of the interlayer distance and hence the interlayer coupling should increase. The

TABLE I. Orbital energies (in eV) obtained from PBE calculations for  $\text{Na}_2\text{SrCo}(\text{PO}_4)_2$  and  $\text{Na}_2\text{BaCo}(\text{PO}_4)_2$ .

	$\text{Na}_2\text{BaCo}(\text{PO}_4)_2$		$\text{Na}_2\text{SrCo}(\text{PO}_4)_2$	
			Co1	Co2
$a_{1g}$	-0.79		-0.90	-0.89
$e'_g$	-0.69		-0.83	-0.82
			-0.80	-0.78
$e_g$	0.01		0.03	0.04
			0.08	0.07

buffer ions not only affect the spacing of the magnetic layers as may be expected, but also have a significant influence on the symmetry. To explain the lower monoclinic symmetry of the Sr compound compared to the Ba compound, the environments of the divalent ions will be compared by calculating the bond valence sum (BVS). In this case, the BVS connects the oxidation state of the alkaline-earth metal to their bond length to the surrounding  $\text{O}^{2-}$  ions. The needed empirical constants were taken from [56]. The resulting BVS, effective coordination, and average bond length are listed in Table II. In analogy to the BVS, the effective or mean coordination is obtained by adding the surrounding atoms with a weight depending on their distance. In  $P2_1/a$ , the smaller Sr ions are coordinated by nine O ions instead of ten as for Ba in  $P\bar{3}m1$ . To ensure the oxidation state of +2 the average bond length has to decrease. This necessitates the tilt and distortion of the octahedra, resulting in the symmetry lowering. The higher average bond length at elevated temperatures allows for the ten-fold coordination and the undistorted structure can form.

An important ramification of the symmetry lowering is the formation of magnetic order with an uncompensated spin component in  $\text{Na}_2\text{SrCo}(\text{PO}_4)_2$ . Such uncompensated components would typically arise from DM interactions that are controlled by the inversion symmetry. Indeed, in the trigonal Ba compound, every Co-Co bond carries an inversion center which is removed in the Sr compound for two of the three bonds of the trian-

TABLE II. Results of the BVS for the SrO and BaO-polyhedra.

	BVS	effective coordination	average bond length ( $\text{\AA}$ )
$\text{Na}_2\text{SrCo}(\text{PO}_4)_2$ 300 K, $P2_1/a$	2.033	9.0	2.7255
$\text{Na}_2\text{SrCo}(\text{PO}_4)_2$ 1025 K, $P\bar{3}m1$	1.678	9.8	2.8932
$\text{Na}_2\text{BaCo}(\text{PO}_4)_2$ 300 K, $P\bar{3}m1$	2.398	10.5	2.9141

TABLE III. Ratio of the Néel temperature  $T_N$  to the average exchange coupling  $J_{av}/k_B$  for several spin-1/2 triangular antiferromagnets.  $J_{av}/k_B = (2J_{xy} + J_z)/3k_B$  and  $J_{av}/k_B = (J + 2J')/3k_B$  for the Co and Cu compounds, respectively.

	$T_N$ (K)	$J_{av}/k_B$ (K)	$k_B T_N/J_{av}$
$\text{Na}_2\text{BaCo}(\text{PO}_4)_2$ [31]	0.14	1.3	0.11
$\text{Ba}_3\text{CoSb}_2\text{O}_9$ [52]	3.8	19.19	0.20
$\text{Cs}_2\text{CuBr}_4$ [53, 54]	1.4	9.0	0.16
$\text{Cs}_2\text{CuCl}_4$ [55]	0.62	2.42	0.26
$\text{Na}_2\text{SrCo}(\text{PO}_4)_2$	0.60	1.32	0.45

gle. The lack of the bond inversion symmetry is a necessary condition for DM interactions and therefore only possible in the Sr compound. DM interactions favor non-collinear spin arrangement because energy is gained when spins become tilted relative to each other. The formation of uncompensated moments is a typical manifestation of non-collinear spin structures driven by DM interactions.

A further consequence of the symmetry lowering is the enhanced  $g$ -tensor anisotropy. In the isotropic case (undistorted  $\text{CoO}_6$  octahedron),  $g = 4.33$  for both field directions. Parallel and perpendicular components of the  $g$  tensor split if distortions are introduced [57]. The increase in the  $g$ -tensor anisotropy is accompanied by the enhancement of the XXZ anisotropy with the anisotropy parameter  $\Delta = J_z/J_{xy} = 2.04 \text{ K}/0.96 \text{ K} = 2.13$  estimated from the Curie-Weiss temperatures. In comparison, we determined the anisotropy parameter of the Ba compound to be lower,  $\Delta = J_z/J_{xy} = 1.68 \text{ K}/1.11 \text{ K} = 1.51$  [31], which is in good agreement with the calculated literature values [50].

Table III lists the ratio  $k_B T_N/J_{av}$  for several spin-1/2 triangular antiferromagnets. Compared to other compounds with  $k_B T_N/J_{av}$  of around 0.2, the Ba compound has the lowest ratio, whereas the Sr compound has the highest ratio. Despite very similar exchange couplings, the Néel temperature is over four times larger in the Sr compound. We ascribe this difference to three possible effects. First, the smaller size of  $\text{Sr}^{2+}$  leads to a stronger interlayer coupling and increases  $T_N$ . Second, the enhanced XXZ anisotropy acts to suppress quantum fluctuations and increase  $T_N$ . At first glance, the  $120^\circ$  order requires an easy-plane anisotropy and would be disfavoured by the easy-axis one, but it can also be compatible with the  $J_z/J_{xy} > 1$  regime if one of the spins aligns with the  $c$  axis, resulting in the Y-type order [47]. Such an order is favored by the easy-axis anisotropy and becomes progressively more stable when  $J_z/J_{xy}$  increases. Finally, the third potentially important effect is the distortion of the triangular spin lattice in monoclinic  $\text{Na}_2\text{SrCo}(\text{PO}_4)_2$ , as compared to  $\text{Na}_2\text{BaCo}(\text{PO}_4)_2$  with its higher trigonal symmetry.

This difference between the Sr and Ba compounds can

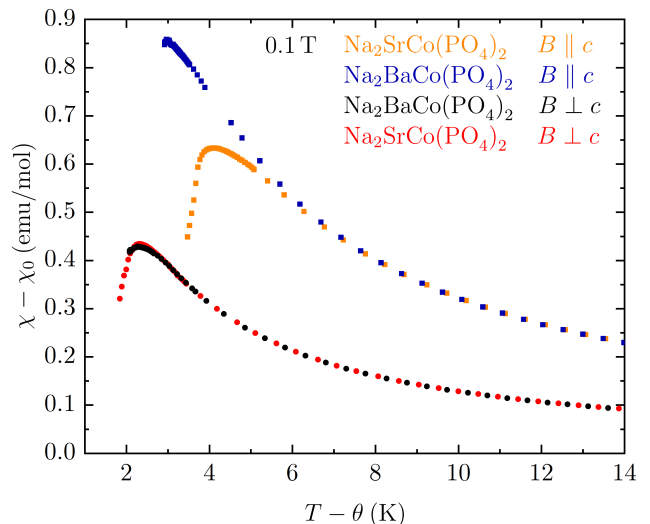


FIG. 11. Comparison of the rescaled susceptibilities of  $\text{Na}_2\text{SrCo}(\text{PO}_4)_2$  and  $\text{Na}_2\text{BaCo}(\text{PO}_4)_2$  [31] for both field directions at 0.1 T. Deviations are prominent at low temperatures.

be also visualized by re-scaling magnetic susceptibilities so that they match in the paramagnetic regime (Fig. 11). At low temperatures, the largest deviation between the Sr and Ba compounds is seen for  $H \parallel c$ . It further indicates that easy-axis anisotropy becomes stronger in the Sr compound, and that spins in the magnetically ordered state are primarily directed along  $c$ . More generally, we see that even a small monoclinic distortion can have a strong influence on the ordering temperature of triangular antiferromagnets. Whereas the ratio  $k_B T_N/J_{av}$  of  $\text{Na}_2\text{SrCo}(\text{PO}_4)_2$  is higher than in other TLAFs,  $k_B T_N/J_{av}$  of  $\text{Na}_2\text{BaCo}(\text{PO}_4)_2$  is lower. One interesting possibility is that a structural distortion is present in the Ba compound too, but contrary to the Sr compound this distortion reduces  $T_N$ . Detailed studies of the  $\text{Na}_2\text{BaCo}(\text{PO}_4)_2$  crystal structure could shed further light on this scenario.

In this paper, we investigated the compound  $\text{Na}_2\text{SrCo}(\text{PO}_4)_2$ , a close analog of the recently studied quantum spin liquid candidate  $\text{Na}_2\text{BaCo}(\text{PO}_4)_2$ . It crystallizes in the monoclinic  $P2_1/a$  space group. At around 650 K, the structure transforms into  $C2/m$  and further evolves toward trigonal with increasing temperature until the transition is completed above 1025 K. The change in symmetry compared to  $\text{Na}_2\text{BaCo}(\text{PO}_4)_2$  has several repercussions for the magnetic behavior. DM interactions are now possible and lead to the formation of an uncompensated moment in the  $ab$  plane. Distortions of the  $\text{CoO}_6$  octahedra beyond trigonal, which are possible in the lower symmetry, lead to an increase of the  $g$  anisotropy and to a larger XXZ anisotropy. The distortion of the triangular lattice reduces the amount of frustration in the system. These aspects lead together with the increase of the interlayer coupling to a four times

higher Néel temperature in  $\text{Na}_2\text{SrCo}(\text{PO}_4)_2$  compared to  $\text{Na}_2\text{BaCo}(\text{PO}_4)_2$ .

*Note added:* upon completing this manuscript we became aware of the concurrent work on  $\text{Na}_2\text{SrCo}(\text{PO}_4)_2$  that reports polycrystalline samples and their thermodynamic properties down to 2 K [58]. The room-temperature monoclinic ( $P2_1/a$ ) crystal structure reported in that work is in full agreement with our results.

## ACKNOWLEDGMENTS

We acknowledge ESRF for providing beamtime for this project, and thank Andy Fitch, Catherine Dejoie, and Ola Grendal for their help during the data collection. AT thanks Mike Zhitomirsky and Oleg Janson for a fruitful discussion. This work was supported by the German Research Foundation (DFG) via Project No. 107745057 (TRR80).

\* vera.bader@uni-a.de

† altsirlin@gmail.com

- [1] P. Anderson, Resonating valence bonds: A new kind of insulator?, *Mater. Res. Bull.* **8**, 153 (1973).
- [2] D. A. Huse and V. Elser, Simple Variational Wave Functions for Two-Dimensional Heisenberg Spin-1/2 Antiferromagnets, *Phys. Rev. Lett.* **60**, 2531 (1988).
- [3] L. Capriotti, A. E. Trumper, and S. Sorella, Long-Range Néel Order in the Triangular Heisenberg Model, *Phys. Rev. Lett.* **82**, 3899 (1999).
- [4] D. Yamamoto, G. Marmorini, and I. Danshita, Quantum Phase Diagram of the Triangular-Lattice  $XXZ$  Model in a Magnetic Field, *Phys. Rev. Lett.* **112**, 127203 (2014).
- [5] Y. Li, P. Gegenwart, and A. A. Tsirlin, Spin liquids in geometrically perfect triangular antiferromagnets, *J. Phys.: Condens. Matter* **32**, 224004 (2020).
- [6] Z. Zhu and S. R. White, Spin liquid phase of the  $S = \frac{1}{2}J_1 - J_2$  Heisenberg model on the triangular lattice, *Phys. Rev. B* **92**, 041105(R) (2015).
- [7] Y. Iqbal, W.-J. Hu, R. Thomale, D. Poilblanc, and F. Becca, Spin liquid nature in the Heisenberg  $J_1 - J_2$  triangular antiferromagnet, *Phys. Rev. B* **93**, 144411 (2016).
- [8] J. Iaconis, C. Liu, G. B. Halász, and L. Balents, Spin Liquid versus Spin Orbit Coupling on the Triangular Lattice, *SciPost Phys.* **4**, 003 (2018).
- [9] Q. Luo, S. Hu, B. Xi, J. Zhao, and X. Wang, Ground-state phase diagram of an anisotropic spin- $\frac{1}{2}$  model on the triangular lattice, *Phys. Rev. B* **95**, 165110 (2017).
- [10] M. Zhang, C. Wang, S. Dong, H. Zhang, Y. Han, and L. He, Projected entangled pair states study of anisotropic-exchange magnets on the triangular lattice, *Phys. Rev. B* **105**, 024411 (2022).
- [11] Z. Zhu, P. A. Maksimov, S. R. White, and A. L. Chernyshev, Topography of Spin Liquids on a Triangular Lattice, *Phys. Rev. Lett.* **120**, 207203 (2018).
- [12] P. A. Maksimov, Z. Zhu, S. R. White, and A. L. Chernyshev, Anisotropic-Exchange Magnets on a Triangular Lattice: Spin Waves, Accidental Degeneracies, and Dual Spin Liquids, *Phys. Rev. X* **9**, 021017 (2019).
- [13] R. Zhong, S. Guo, G. Xu, Z. Xu, and R. J. Cava, Strong quantum fluctuations in a quantum spin liquid candidate with a Co-based triangular lattice, *Proc. Natl. Acad. Sci. U.S.A.* **116**, 14505 (2019).
- [14] S. Lee, C. H. Lee, A. Berlie, A. D. Hillier, D. T. Adroja, R. Zhong, R. J. Cava, Z. H. Jang, and K.-Y. Choi, Temporal and field evolution of spin excitations in the disorder-free triangular antiferromagnet  $\text{Na}_2\text{BaCo}(\text{PO}_4)_2$ , *Phys. Rev. B* **103**, 024413 (2021).
- [15] A. Möller, N. E. Amunke, P. Daniel, B. Lorenz, C. R. dela Cruz, M. Gooch, and P. C. W. Chu,  $A\text{Ag}_2M[\text{VO}_4]_2$  ( $A = \text{Ba}, \text{Sr}; M = \text{Co}, \text{Ni}$ ): A series of ferromagnetic insulators, *Phys. Rev. B* **85**, 214422 (2012).
- [16] N. Li, Q. Huang, X. Yue, W. Chu, Q. Chen, E. Choi, X. Zhao, H. Zhou, and X. Sun, Possible itinerant excitations and quantum spin state transitions in the effective spin-1/2 triangular-lattice antiferromagnet  $\text{Na}_2\text{BaCo}(\text{PO}_4)_2$ , *Nature Comm.* **11**, 4216 (2020).
- [17] C. Wellm, W. Roscher, J. Zeisner, A. Alfonsov, R. Zhong, R. J. Cava, A. Savoyant, R. Hayn, J. van den Brink, B. Büchner, O. Janson, and V. Kataev, Frustration enhanced by Kitaev exchange in a  $\tilde{J}_{\text{eff}} = \frac{1}{2}$  triangular antiferromagnet, *Phys. Rev. B* **104**, L100420 (2021).
- [18] T. Ono, H. Tanaka, H. Aruga Katori, F. Ishikawa, H. Mitamura, and T. Goto, Magnetization plateau in the frustrated quantum spin system  $\text{Cs}_2\text{CuBr}_4$ , *Phys. Rev. B* **67**, 104431 (2003).
- [19] N. A. Fortune, S. T. Hannahs, Y. Yoshida, T. E. Sherrill, T. Ono, H. Tanaka, and Y. Takano, Cascade of Magnetic-Field-Induced Quantum Phase Transitions in a Spin- $\frac{1}{2}$  Triangular-Lattice Antiferromagnet, *Phys. Rev. Lett.* **102**, 257201 (2009).
- [20] J. Alicea, A. V. Chubukov, and O. A. Starykh, Quantum Stabilization of the 1/3-Magnetization Plateau in  $\text{Cs}_2\text{CuBr}_4$ , *Phys. Rev. Lett.* **102**, 137201 (2009).
- [21] T. Susuki, N. Kurita, T. Tanaka, H. Nojiri, A. Matsuo, K. Kindo, and H. Tanaka, Magnetization Process and Collective Excitations in the  $s = 1/2$  Triangular-Lattice Heisenberg Antiferromagnet  $\text{Ba}_3\text{CoSb}_2\text{O}_9$ , *Phys. Rev. Lett.* **110**, 267201 (2013).
- [22] R. Rawl, L. Ge, H. Agrawal, Y. Kamiya, C. R. dela Cruz, N. P. Butch, X. F. Sun, M. Lee, E. S. Choi, J. Oitmaa, C. D. Batista, M. Mourigal, H. D. Zhou, and J. Ma,  $\text{Ba}_8\text{CoNb}_6\text{O}_{24}$ : A spin- $\frac{1}{2}$  triangular-lattice Heisenberg antiferromagnet in the two-dimensional limit, *Phys. Rev. B* **95**, 060412(R) (2017).
- [23] Y. Cui, J. Dai, P. Zhou, P. S. Wang, T. R. Li, W. H. Song, J. C. Wang, L. Ma, Z. Zhang, S. Y. Li, G. M. Luke, B. Normand, T. Xiang, and W. Yu, Mermin-Wagner physics, ( $H, T$ ) phase diagram, and candidate quantum spin-liquid phase in the spin- $\frac{1}{2}$  triangular-lattice antiferromagnet  $\text{Ba}_8\text{CoNb}_6\text{O}_{24}$ , *Phys. Rev. Mater.* **2**, 044403 (2018).
- [24] Bruker (2012), *APEX2. Bruker AXS Inc., Madison, Wisconsin, USA.*
- [25] L. Krause, R. Herbst-Irmer, G. Sheldrick, and D. Stalke, Comparison of silver and molybdenum microfocus X-ray sources for single-crystal structure determination, *J.*



- Appl. Crystallogr.* **48**, 3 (2015).
- [26] V. Petříček, M. Dušek, and L. Palatinus, Crystallographic Computing System JANA2006: General features, *Z. Krist.* **229**, 345 (2014).
- [27] See Supplemental Material at <https://journals.aps.org/prb/supplemental/10.1103/PhysRevB.106.054415> for details and results of SCXRD experiments at room temperature and PXRD experiments at 800 K and 1025 K, and fit of the zero-field heat capacity data.
- [28] K. Momma and F. Izumi, *VESTA3* for three-dimensional visualization of crystal, volumetric and morphology data, *J. Appl. Crystallogr.* **44**, 1272 (2011).
- [29] K. Koepernik and H. Eschrig, Full-potential nonorthogonal local-orbital minimum-basis band-structure scheme, *Phys. Rev. B* **59**, 1743 (1999).
- [30] J. P. Perdew, K. Burke, and M. Ernzerhof, Generalized Gradient Approximation Made Simple, *Phys. Rev. Lett.* **77**, 3865 (1996).
- [31] V. P. Bader *et al.* (unpublished).
- [32] V. P. Bader, A. Fitch, and A. A. Tsirlin, High-resolution x-ray diffraction on the triangular antiferromagnet  $\text{Na}_2\text{SrCo}(\text{PO}_4)_2$ , European Synchrotron Radiation Facility (ESRF), [10.15151/ESRF-DC-885525061](https://doi.org/10.15151/ESRF-DC-885525061) (2022).
- [33] L. D. Sanjeewa, V. O. Garlea, M. A. McGuire, M. Frontzek, C. D. McMillen, K. Fulle, and J. W. Kolis, Investigation of a Structural Phase Transition and Magnetic Structure of  $\text{Na}_2\text{BaFe}(\text{VO}_4)_2$ : A Triangular Magnetic Lattice with a Ferromagnetic Ground State, *Inorg. Chem.* **56**, 14842 (2017).
- [34] L. D. Sanjeewa, V. O. Garlea, M. A. McGuire, C. D. McMillen, and J. W. Kolis, Magnetic Ground State Crossover in a Series of Glaserite Systems with Triangular Magnetic Lattices, *Inorg. Chem.* **58**, 2813 (2019).
- [35] A. Reuß, V. Ksenofontov, J. Tapp, D. Wulferding, P. Lemmens, M. Panthöfer, and A. Möller, Screw-Type Motion and Its Impact on Cooperativity in  $\text{BaNa}_2\text{Fe}[\text{VO}_4]_2$ , *Inorg. Chem.* **57**, 6300 (2018).
- [36] L. D. Sanjeewa, C. D. McMillen, D. Willett, G. Chumanov, and J. W. Kolis, Hydrothermal synthesis of single crystals of transition metal vanadates in the glaserite phase, *J. Solid State Chem.* **236**, 61 (2016).
- [37] J. Tapp, C. R. dela Cruz, M. Bratsch, N. E. Amuneke, L. Postulka, B. Wolf, M. Lang, H. O. Jeschke, R. Valentí, P. Lemmens, and A. Möller, From magnetic order to spin-liquid ground states on the  $s = \frac{3}{2}$  triangular lattice, *Phys. Rev. B* **96**, 064404 (2017).
- [38] V. P. Bader, O. G. Grendal, and A. A. Tsirlin, High-resolution x-ray diffraction on the triangular antiferromagnet  $\text{Na}_2\text{SrCo}(\text{PO}_4)_2$ , European Synchrotron Radiation Facility (ESRF), [10.15151/ESRF-DC-885525164](https://doi.org/10.15151/ESRF-DC-885525164) (2022).
- [39] A. Boukhris, M. Hidouri, B. Glorieux, and M. B. Amara, Correlation between structure and photoluminescence of the europium doped glaserite-type phosphate  $\text{Na}_2\text{SrMg}(\text{PO}_4)_2$ , *Mater. Chem. Phys.* **137**, 26 (2012).
- [40] M. V. Gvozdkova, P.-E. Melchy, and M. E. Zhitomirsky, Magnetic phase diagrams of classical triangular and kagome antiferromagnets, *J. Phys. Condens. Matter* **23**, 164209 (2011).
- [41] M. Li, A. Zelenskiy, J. A. Quilliam, Z. L. Dun, H. D. Zhou, M. L. Plumer, and G. Quirion, Magnetoelastic coupling and the magnetization plateau in  $\text{Ba}_3\text{CoSb}_2\text{O}_9$ , *Phys. Rev. B* **99**, 094408 (2019).
- [42] D. C. Johnston, R. K. Kremer, M. Troyer, X. Wang, A. Klümper, S. L. Bud'ko, A. F. Panchula, and P. C. Canfield, Thermodynamics of spin  $S=1/2$  antiferromagnetic uniform and alternating-exchange Heisenberg chains, *Phys. Rev. B* **61**, 9558 (2000).
- [43] J. S. Griffith, Octahedral complexes. Part 1.—Magnetic susceptibilities in the first transition series, *Trans. Faraday Soc.* **54**, 1109 (1958).
- [44] M. Tamura and R. Kato, Magnetic susceptibility of  $\beta'$ - $[\text{Pd}(\text{dmit})_2]$  salts ( $\text{dmit} = 1, 3\text{-dithiol-2-thione-4, 5-dithiolate, C}_3\text{S}_5$ ): evidence for frustration in spin-1/2 Heisenberg antiferromagnets on a triangular lattice, *J. Phys.: Condens. Matter* **14**, L729 (2002).
- [45] G. Gitgeatpong, Y. Zhao, M. Avdeev, R. O. Piltz, T. J. Sato, and K. Matan, Magnetic structure and Dzyaloshinskii-Moriya interaction in the  $s = \frac{1}{2}$  helical-honeycomb antiferromagnet  $\alpha\text{-Cu}_2\text{V}_2\text{O}_7$ , *Phys. Rev. B* **92**, 024423 (2015).
- [46] G. Gitgeatpong, M. Suewattana, S. Zhang, A. Miyake, M. Tokunaga, P. Chanlert, N. Kurita, H. Tanaka, T. J. Sato, Y. Zhao, and K. Matan, High-field magnetization and magnetic phase diagram of  $\alpha\text{-Cu}_2\text{V}_2\text{O}_7$ , *Phys. Rev. B* **95**, 245119 (2017).
- [47] D. Yamamoto, G. Marmorini, M. Tabata, K. Sakakura, and I. Danshita, Magnetism driven by the interplay of fluctuations and frustration in the easy-axis triangular XXZ model with transverse fields, *Phys. Rev. B* **100**, 140410(R) (2019).
- [48] K. M. Ranjith, S. Luther, T. Reimann, B. Schmidt, P. Schlender, J. Sichelschmidt, H. Yasuoka, A. M. Strydom, Y. Skourski, J. Wosnitza, H. Kühne, T. Doert, and M. Baenitz, Anisotropic field-induced ordering in the triangular-lattice quantum spin liquid  $\text{NaYbSe}_2$ , *Phys. Rev. B* **100**, 224417 (2019).
- [49] N. Elstner, R. R. P. Singh, and A. P. Young, Finite temperature properties of the spin-1/2 Heisenberg antiferromagnet on the triangular lattice, *Phys. Rev. Lett.* **71**, 1629 (1993).
- [50] Y. Gao, Y.-C. Fan, H. Li, F. Yang, X.-T. Zeng, X.-L. Sheng, R. Zhong, Y. Qi, Y. Wan, and W. Li, Spin Supersolidity in Nearly Ideal Easy-axis Triangular Quantum Antiferromagnet  $\text{Na}_2\text{BaCo}(\text{PO}_4)_2$ , [10.48550/ARXIV.2202.05242](https://doi.org/10.48550/ARXIV.2202.05242) (2022).
- [51] H. Liu, Towards Kitaev spin liquid in 3d transition metal compounds, *Int. J. Mod. Phys. B* **35**, 2130006 (2021).
- [52] Y. Kamiya, L. Ge, T. Hong, Y. Qiu, D. L. Quintero-Castro, Z. Lu, H. B. Cao, M. Matsuda, E. S. Choi, B. C. D., M. Mourigal, H. D. Zhou, and J. Ma, The nature of spin excitations in the one-third magnetization plateau phase of  $\text{Ba}_3\text{CoSb}_2\text{O}_9$ , *Nature Comm.* **9**, 2666 (2018).
- [53] T. Ono, H. Tanaka, O. Kolomiyets, H. Mitamura, F. Ishikawa, T. Goto, K. Nakajima, A. Oosawa, Y. Koike, K. Kakurai, J. Klenke, P. Smeibidle, M. Meißner, R. Coldea, A. D. Tennant, and J. Ollivier, Field-Induced Phase Transitions Driven by Quantum Fluctuation in  $S = 1/2$  Anisotropic Triangular Antiferromagnet  $\text{Cs}_2\text{CuBr}_4$ , *Progr. Theor. Phys.* **159**, 217 (2005).
- [54] S. A. Zvyagin, D. Kamenskiy, M. Ozerov, J. Wosnitza, M. Ikeda, T. Fujita, M. Hagiwara, A. I. Smirnov, T. A. Soldatov, A. Y. Shapiro, J. Krzystek, R. Hu, H. Ryu, C. Petrovic, and M. E. Zhitomirsky, Direct Determination of Exchange Parameters in  $\text{Cs}_2\text{CuBr}_4$  and  $\text{Cs}_2\text{CuCl}_4$ : High-Field Electron-Spin-Resonance Studies, *Phys. Rev. Lett.* **112**, 077206 (2014).

- [55] R. Coldea, D. A. Tennant, A. M. Tsvelik, and Z. Tylczynski, Experimental Realization of a 2D Fractional Quantum Spin Liquid, *Phys. Rev. Lett.* **86**, 1335 (2001).
- [56] I. D. Brown and D. Altermatt, Bond-valence parameters obtained from a systematic analysis of the Inorganic Crystal Structure Database, *Acta Crystallogr. Sect. B* **41**, 244 (1985).
- [57] A. Abragam and B. Bleaney, *Electron Paramagnetic Resonance of Transition Ions*, Oxford University Press (1970).
- [58] C. Zhang, Q. Xu, X.-T. Zeng, C. Lyu, Z. Lin, J. Hao, S. Deng, L. He, Y. Xiao, Y. Ye, Z. Chen, X.-L. Sheng, and W. Jin, Doping-induced structural transformation in the spin-1/2 triangular-lattice antiferromagnet  $\text{Na}_2\text{Ba}_{1-x}\text{Sr}_x\text{Co}(\text{PO}_4)_2$ , *J. Alloys Compd.* **905**, 164147 (2022).